Journal of Power Sources 187 (2009) 487–492

Contents lists available at ScienceDirect

Journal of Power Sources

journal homepage: www.elsevier.com/locate/jpowsour

Characterization of internal wetting in polymer electrolyte membrane gas diffusion layers

Perry Cheung, Joseph D. Fairweather, Daniel T. Schwartz*

Electrochemical Materials and Interfaces Laboratory, Department of Chemical Engineering, Box 351750, University of Washington, Seattle, WA 98195-1750, United States

ARTICLE INFO

Article history:
Received 9 September 2008
Received in revised form 27 October 2008
Accepted 5 November 2008
Available online 18 November 2008

Keywords:
PEM fuel cells
Gas diffusion layers
Gas diffusion electrode
Capillary pressure
Wetting properties
Water flooding

ABSTRACT

Capillary pressure vs. saturation ($P_C(S_L)$) curves are fundamental to understanding liquid water transport and flooding in PEM gas diffusion layers (GDLs). $P_C(S_L)$ curves convolute the influence of GDL pore geometry and internal contact angles at the three-phase liquid/solid/gas boundary. Even simple GDL materials are a spatially non-uniform mixture of carbon fiber and binder, making a Gaussian distribution of contact angles likely, based on the Cassie–Baxter equation. For a given Gaussian contact angle distribution with mean (θ_{Mean}) and standard deviation (σ), a realistic $P_C(S_L)$ curve can be computed using a bundle of capillaries model and GDL pore size distribution data. As expected, computed $P_C(S_L)$ curves show that θ_{Mean} sets the overall hydrophilic ($\theta_{Mean} < 90^\circ$) or hydrophobic ($\theta_{Mean} > 90^\circ$) character of the GDL (i.e., liquid saturation level at a given capillary pressure), and σ affects the slope of the $P_C(S_L)$ curve. The capillary bundle model also can be used with (θ_{Mean}, σ) as unknown parameters that are best-fit to experimentally acquired $P_C(S_L)$ and pore size distribution data to find (θ_{Mean}, σ) values for actual GDL materials. To test this, pore size distribution data was acquired for Toray TGP-H-090 along with hysteretic liquid and gas intrusion capillary pressure curve data. High quality best-fits were found between the model and combined datasets, with GDL liquid intrusion showing fairly neutral internal surface wetting properties ($\theta_{Mean} = 92^\circ$ and $\sigma = 10^\circ$) whereas gas intrusion displayed a hydrophilic character ($\theta_{Mean} = 52^\circ$ and $\sigma = 8^\circ$). External liquid advancing and receding contact angles were also measured on this same material and they also showed major hysteresis. The new methods described here open the door for better understanding of the link between GDL material processing and the wetting properties that affect flooding.

© 2008 Elsevier B.V. All rights reserved.

1. Introduction

Polymer electrolyte membrane fuel cells (PEMFCs) show promise as power sources for a range of applications owing to their high power density, low pollution, and low noise [1,2]. However, water management continues to pose a considerable challenge [2–6]. When the PEMFC is operated at high current densities, liquid water floods and blocks access to the catalyst sites from the reactant gases [1,4–8]. Part of the solution to liquid water management is the design of the porous gas diffusion layer (GDL) [2,8–10]. Manufacturing GDLs to have mixed hydrophobic/hydrophilic pores, in theory, promotes both gas transport to and liquid removal from the catalyst layer [2]. This mixture of hydrophobic/hydrophilic pores is accomplished by treating the moderately wetting fibrous carbon substrates with polytetraflourethylene (PTFE or otherwise known as Teflon®), where an empirical rule of thumb is to apply 5–30 wt% PTFE for optimal water management in GDLs [9,11,12].

One of the key properties of a GDL that gets modified by Teflon® treatment is the capillary pressure versus liquid saturation behavior [8]. Capillary pressure (P_C) is defined here as

$$P_C = P_L - P_G \quad (1)$$

where P_L and P_G are the liquid and gas phase pressures, respectively. Capillary pressure is a thermodynamic property that relates the liquid–vapor interface to surface properties and pore geometries via the modified Young–Laplace equation [13]:

$$P_C = -\frac{2\gamma \cos\theta}{R_{Eff}} \quad (2)$$

where γ is the surface tension of the liquid–vapor interface, θ is the contact angle of the liquid with the solid (measured within the liquid phase), and R_{Eff} is the effective pore radius in an equivalent cylindrical capillary. For liquid water, $\theta > 90^\circ$ defines a hydrophobic material whereas $\theta < 90^\circ$ is a hydrophilic material. From Eqs. (1) and (2), one sees that Teflon® rich regions in the GDL are hydrophobic (θ ranging from 98° to 112° for water on PTFE [7,14,15]) and are expected to have a positive P_C, whereas the carbon rich regions are hydrophilic (with θ reported to be 80° [7] or 86° [14] for water on graphite) and are expected to display a negative P_C.

* Corresponding author.
E-mail address: dts@u.washington.edu (D.T. Schwartz).

0378-7753/$ – see front matter © 2008 Elsevier B.V. All rights reserved.
doi:10.1016/j.jpowsour.2008.11.036

GDL capillary pressure measurements at different liquid saturations (S_L) have shown a mixture of both hydrophilic and hydrophobic surfaces, even when no Teflon is added to the structure [16–22], where liquid saturation is defined as

$$S_L = \frac{V_L}{V_{Pore}} = \frac{V_L}{\varepsilon V_{Total}} \quad (3)$$

with V_L the liquid volume, V_{Pore} the pore volume, ε the porosity, and V_{Total} the total material volume. The resulting GDL capillary pressure vs. liquid saturation curves (P_C vs. S_L, or $P_C(S_L)$) provide a constitutive relationship describing the integrated capillary properties (internal wetting and pore geometry) in the porous material. Additionally, these $P_C(S_L)$ curves are dependent on the history and whether the liquid–vapor interface is advancing (liquid intrusion) over an unwetted surface or receding (gas intrusion) over a wetted surface, otherwise known as hysteresis [13,23–25].

$P_C(S_L)$ measurement is an emerging area of research in GDLs. Gostick et al. [16] used contact porosimetry [26] and measured the $P_C(S_L)$ curves for gas intrusion using water in hydrophilic pores only. Kumbur et al. [17–19] also used contact porosimetry to measure $P_C(S_L)$ curves for gas intrusion using water in hydrophilic pores but also looked at the effects of compression and temperature. Fairweather et al. [20] developed a microfluidic device and was the first to measure the $P_C(S_L)$ curves for both liquid and gas intrusion while probing both hydrophilic and hydrophobic pores. Gostick et al. [21] recently used a similar method to Fairweather et al. to probe both hydrophilic and hydrophobic pores by controlling the gas phase pressure; they observed the same hysteresis when cycling between liquid and gas intrusion. Nguyen et al. [22] used a volume–displacement technique and optically tracked the change in liquid volume but did not observe any hysteresis in their $P_C(S_L)$ curves. Although $P_C(S_L)$ curves provide a means of determining the hydrophilic and hydrophobic character of the material, the specific pore size and internal wetting properties are convoluted through Eq. (2).

Weber et al. [7] is the first to combine independent pore size distribution data with the mixed wetting properties of the different materials present in GDLs. Their model consisted of a bundle of capillaries with the GDL pore size distribution determined from mercury intrusion porosimetry (MIP) [27,28] data. Each pore was randomly assigned a single discrete hydrophilic or hydrophobic contact angle in proportion to the amount of hydrophilic/hydrophobic material present in the GDL. This model was then capable of determining the extent of saturation at different capillary pressures, with $P_C(S_L)$ curves showing both wetting and non-wetting characteristics. Despite the significant advance represented by Weber's work, the use of single-valued contact angles representing the wetting and non-wetting surfaces of the material produced an aphysical feature, namely a discontinuity at liquid saturations where all the hydrophilic pores were filled. Recently, Sinha et al. [6] used a uniform distribution of contact angles to understand the behavior of water in GDLs having mixed wetting properties. A uniform contact angle distribution is a computationally straightforward way to remove aphysical features in the capillary behavior of GDLs, but the most realistic representation is likely to be somewhere between Weber's [7] single values and Sinha's [6] uniform values. Specifically, a material with chemical heterogeneous surfaces will show an averaged wetting described by the Cassie–Baxter equation [14,29,30]:

$$\cos\theta_{Obs} = f_1 \cos\theta_1 + (1 - f_1)\cos\theta_2 \quad (4)$$

where θ_{Obs} is the observed contact angle, θ_1 and θ_2 the contact angle of the two different surfaces, and f_1 the fractional coverage of surface 1. Moreover, intrinsic roughness adds variability to the contact angle, as described by Wenzel's equation [14,24,29,31]:

$$\cos\theta_{Obs} = r \cos\theta_o \quad (5)$$

where r is the rugosity or roughness factor and θ_o is the intrinsic contact angle. Thus, for a GDL with chemical heterogeneity and roughness generated by Teflon® or binder [11] that is randomly distributed throughout the porous geometry, one would expect a Gaussian distribution of contact angles.

In this work we present a method for analyzing internal surface wetting in GDLs using independent data from MIP and $P_C(S_L)$ measurements via a bundle of capillaries model that assumes a realistic Gaussian wetting distribution. This approach carefully deconvolutes, for the first time, the intrinsic material properties from the porous geometry in a manufactured GDL, providing the kind of data that can guide better GDL designs.

Table 1
Physical properties for the 24 mm diameter Toray TGP-H-090 GDL sample.

Property	Value
Thickness (L) (μm)	280[a]
Porosity (ε)	0.78[a]
V_{Pore} (μL)	99
Advancing contact angle, external ($\theta_{Adv,Ext}$) (°)	153°
Receding contact angle, external ($\theta_{Rec,Ext}$) (°)	47°

[a] Denotes manufactured supplied properties.

2. Experimental methods

2.1. Materials

A commercially available as-received untreated Toray TGP-H-090 GDL sample (Toray CFA, Flower Mound, TX) was investigated. External advancing and receding contact angle measurements were performed with a Rame-Hart Model 100 contact angle goniometer to determine the extent of hysteresis. Table 1 lists the physical properties of the sample.

2.2. Microfluidic system

A schematic of the apparatus used to measure capillary pressure in the GDL samples is shown in Fig. 1. A liquid manifold (labeled A) connects a syringe pump to the GDL sample housing (labeled B) and a differential pressure sensor (labeled P_C). A gas manifold (labeled C) connects the top of the sample housing to a second pressure sensor (labeled P_G) and two gas lines providing humidified air and a vacuum source. The faces between the two manifolds and

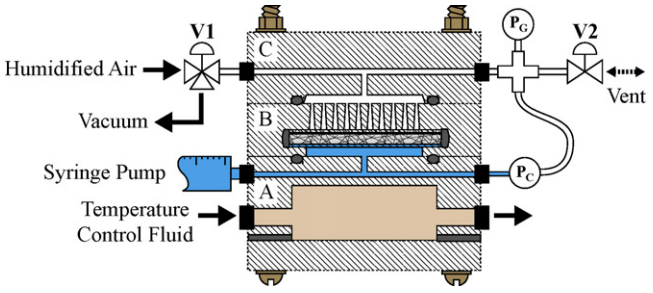

Fig. 1. The cell used to measure capillary pressure in GDL materials. A syringe pump is used to control liquid movement into and out of the GDL sample. A liquid manifold (A) connects the pump to the bottom of the GDL sample housing (B), and a gas manifold (C) connects the top of the sample to lines for vacuum and humidified air, selected by valve V1. A pressure sensor (P_C) measures the difference between the liquid and gas pressures. A second sensor (P_G) and a needle valve (V2) are used to set the vacuum pressure during the initial fill procedure. A heating/cooling recirculator passes temperature control fluid through the liquid manifold.

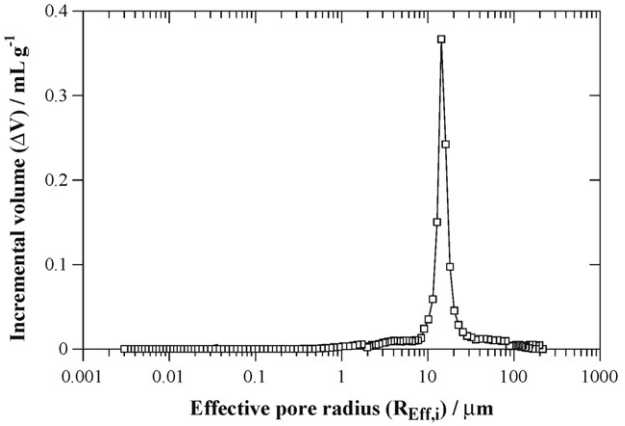

Fig. 2. Pore size distribution of Toray TGP-H-090 showing the incremental volume (ΔV) contained at each effective radii ($R_{Eff,i}$).

the sample housing are sealed by o-rings. The GDL sample itself is sandwiched between a hydrophilic membrane on the liquid side and a hydrophobic membrane on the gas side to provide a gas barrier and liquid barrier, respectively. The construction details of the GDL sample housing have been described previously [20].

2.3. Operation

Before each experiment, the cell is filled under vacuum; the aspirator line is selected with a three way valve (labeled V1 in Fig. 1), the air pressure is set to ~4 kPa absolute using the needle valve (labeled V2), and the liquid side of the cell is filled with degassed water from the syringe pump. The liquid manifold, hydrophilic membrane, and GDL sample are all wetted, while the hydrophobic membrane provides an effective barrier to the water. When the GDL sample is saturated indicated by $P_C \geq 30$ kPa, the vacuum is released, and a testing procedure is followed similar to one previously reported [20]. To evenly wet the GDL sample, the syringe pump repeatedly cycles liquid water into and out of the GDL sample at a constant flow rate of 10 μL min^{-1}. During cycling the difference between the liquid and gas pressures is measured using the "P_C" pressure sensor, with the volume limits chosen such that the measured P_C oscillates between −30 and +30 kPa. After at least three constant rate cycles, a stepwise cycle is performed and the $P_C(S_L)$ curve is determined as described previously [20]. Air is humidified by passing it through a gas sparge bottle and supplied to the gas manifold, to minimize evaporation from the sample. Cell temperature is controlled by a heating/cooling recirculator bath attached to a heat exchanger built into the liquid manifold. All the data included here were collected at 25 °C for three repeated measurements.

2.4. Mercury intrusion porosimetry (MIP)

Mercury intrusion porosimetry (MIP) was performed on the GDL sample using a Micromeritics AutoPore IV 9500 (Micromeritics Instrument Corporation, Norcross, GA). The pressure range applied ranged from 0.4 to 30,000 psia. At each applied pressure, the incrementally intruded volume (ΔV) of mercury was recorded.

3. Results and analysis

3.1. Pore size distribution from MIP data

Fig. 2 shows the incremental volume (ΔV) associated with each effective pore radius ($R_{Eff,i}$) acquired from MIP data for the Toray TGP-H-090. Following standard procedures, a bundle of capillaries model was used to convert each applied pressure to an $R_{Eff,i}$ via Eq. (2) by assuming $\theta = 130°$ [27]. The majority of the GDL volume occurs in pores of radii near 10 μm. Dividing each ΔV data point in Fig. 2 by the individual pore volume ($\pi R_{Eff,i}^2 L$) at that effective pore radius provides an estimate of the number of capillaries in that size range. Such calculations reveal that large pores ($R_{Eff,i} \sim 10$ μm) occupy most of the volume but are a lot less prevalent in number than smaller pores ($R_{Eff,i} \sim 0.01$ μm), despite the fact that small pores occupy very little volume. We use the data in Fig. 2 directly in our bundle of capillaries model to defines the $R_{Eff,i}$ found in our materials. Thus, by attaching realistic wetting properties (i.e., contact angles) to these capillaries, a $P_C(S_L)$ curve can be generated.

3.2. Contact angle distribution and the $P_C(S_L)$ curve

The contact angle distribution is described by a normalized Gaussian distribution that relates the probability (ψ) of finding a pore with a contact angle θ_j,

$$\psi(\theta_j) = \frac{\exp\{-(\theta_j - \theta_{Mean})^2/2\sigma^2\}}{\sum_{j=1}^{M} \exp\{-(\theta_j - \theta_{Mean})^2/2\sigma^2\}} \quad (6)$$

where θ_{Mean} is the mean contact angle, σ is the standard deviation of the contact angle due to heterogeneity and roughness, and M is the total number of discrete contact angles selected for computational purposes. For all our calculations, $M = 181$ corresponding to θ_j ranging from 0° to 180° separated by integer values. We further assume that $R_{Eff,i}$ and θ_j are uncorrelated, so that we can randomly assign contact angles among all pores computed through independently-acquired MIP data.

With Eqs. (2), (6), and an experimentally measured pore size distribution, we are now in a position to determine the P_C and liquid saturation level for every possible combination of $R_{Eff,i}$ and θ_j. For any given capillary pressure we select ($P_{C,k}$), we identify a filled pore as one that satisfies

$$P_C(R_{Eff,i}, \theta_j) \leq P_{C,k} \quad (7)$$

By marching through every possible $R_{Eff,i}$ and θ_j and cataloging every pore satisfying Eq. (7), the saturation of the GDL at the given $P_{C,k}$ is determined. Algorithmically, the saturation (S_L) is determined by

$$S_L(P_{C,k}) = \frac{\sum_{i=1}^{N}\sum_{j=1}^{M} \Delta V(R_{Eff,i})\psi(\theta_j)F}{\sum_{i=1}^{N} \Delta V(R_{Eff,i})} \quad \begin{cases} F = 1 & \text{if } P_C(R_{Eff,i}, \theta_j) \leq P_{C,k} \\ F = 0 & \text{if } P_C(R_{Eff,i}, \theta_j) > P_{C,k} \end{cases} \quad (8)$$

where N is the total number of pores and F is unity when Eq. (7) is satisfied for a pore and zero otherwise. By systematically increasing the $P_{C,k}$ and determining the corresponding S_L, a $P_C(S_L)$ curve is generated.

One way to use the capillary bundle model is to specify a ψ and determine the $P_C(S_L)$ curve. Fig. 3A shows two sets of ψ distributions, one set (labeled i and ii) has a constant σ of 15° but two different values of θ_{Mean} (70° and 110°) and the other (labeled iii and iv) has a constant θ_{Mean} of 90° but two different values of σ (15° and 30°). Fig. 3B shows the $P_C(S_L)$ curves that result after using these contact angle ψ distributions and the experimental pore size distribution for Toray TGP-H-090 given in Fig. 2. The $P_C(S_L)$ curve for Ψ having $\theta_{Mean} = 70°$ and $\sigma = 15°$ (i) shows approximately 90% of the curve being hydrophilic, consistent with $\theta = 90°$ being 1.3 standard deviations from $\theta_{Mean} = 70°$. Similarly, the $P_C(S_L)$ curve with $\theta_{Mean} = 110°$ and $\sigma = 15°$ (ii) shows approximately 90% of the curve being hydrophobic. Curves (i) and (ii) show that θ_{Mean} mainly shifts the $P_C(S_L)$ curve towards either higher or lower P_C values, for a given S_L. High capillary pressure regions in each curve correspond to the volume of the sample associated with small capillary radii.

When ψ has $\theta_{Mean} = 90°$, curves (iii) and (iv), the GDL has an even split of hydrophilic and hydrophobic pore volume, as expected for

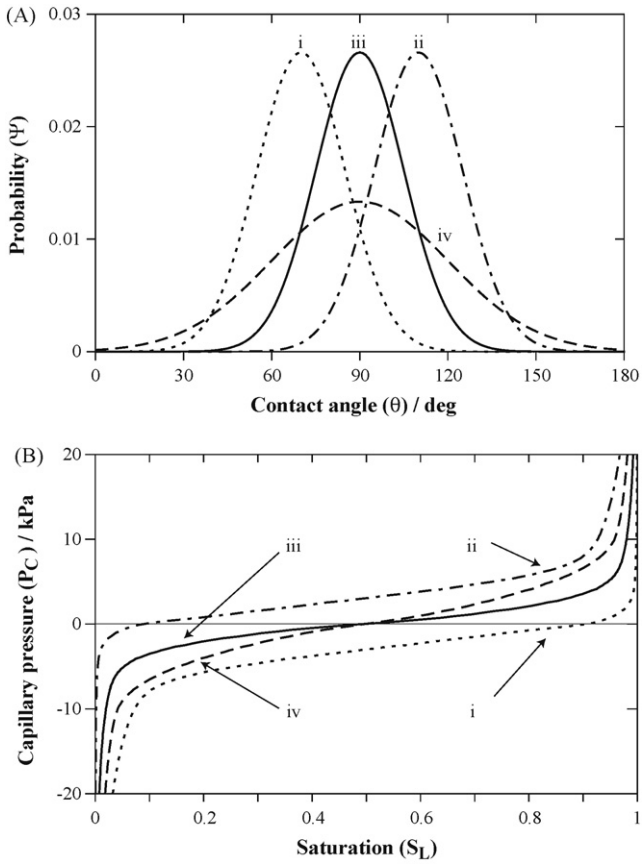

Fig. 3. (A) Four Ψ distributions with different combinations of θ_{Mean} and σ: $\theta_{Mean} = 70^\circ$, $\sigma = 15^\circ$ (i), $\theta_{Mean} = 110^\circ$, $\sigma = 15^\circ$ (ii), $\theta_{Mean} = 90^\circ$, $\sigma = 15^\circ$ (iii), and $\theta_{Mean} = 90^\circ$, $\sigma = 30^\circ$ (iv). (B) The resulting $P_C(S_L)$ curves using the pore size distribution of Toray TGP-H-090 and the different Ψ distributions from A.

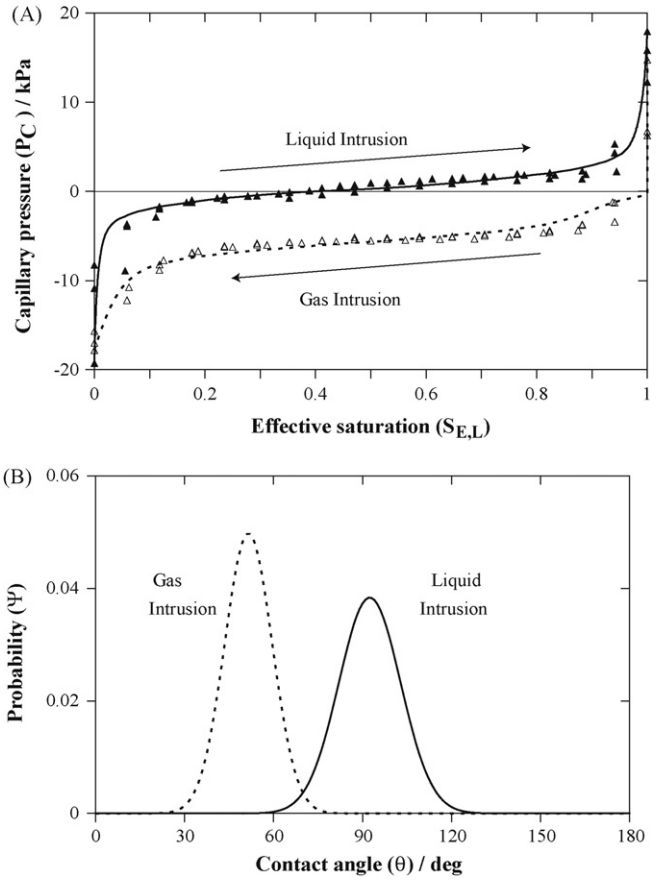

Fig. 4. (A) The experimental $P_C(S_{E,L})$ data (symbols) and model determined best fit $P_C(S_{E,L})$ curves (lines) for Toray TGP-H-090. (B) The resulting Ψ distributions for both liquid (solid line) and gas intrusion (dashed line).

a symmetric contact angle distribution. This is clearly seen in the $P_C(S_L)$ curves by the fact that $P_C = 0$ kPa occurs at $S_L = 50\%$. When σ is increased from 15° (iii) to 30° (iv), one observes that σ largely controls the slope of the $P_C(S_L)$ curve in the middle saturation range. The standard deviation in the contact angle distribution (σ) has a large impact on the portion of the sample pore volume that can generate appreciable capillary pressure deviations from the mean capillary pressure. Specifically, when σ is small and the distribution of contact angels is narrow, only capillaries with small R_{Eff} can generate appreciable pressure deviations, but as σ increases and the distribution includes a wider range of contact angles, the fraction of the pore volume that can generate high capillary pressures also increases. In short, the model results in Fig. 3 show that the value of θ_{Mean} sets the overall hydrophilicity/phobicity of the GDL, whereas σ sets the fraction of the pore volume that deviates significantly from that overall character.

3.3. Best fit to experimental $P_C(S_{E,L})$ curves

Instead of dictating a specific ψ function, the most representative Ψ can be determined from a best fit of the capillary model to experimental $P_C(S_L)$ data using θ_{Mean} and σ as parameters of the fit. The best fit was determined to be the Ψ that yielded the lowest root sum of squared error (RSSE) between the experimental $P_C(S_L)$ data and model. The best fitting protocol was performed using the Optimization Toolbox v.3.1 with Matlab R2007b. The details of the fitting procedure are described in Appendices A and B. The saturations (S_L) have been scaled to an effective saturation ($S_{E,L}$) that ranges from 0 to 1 in order to remove the effects of the residual gas saturation (S_R) and irreducible liquid saturation (S_{IR}) [13]:

$$S_{E,L} = \frac{S_L - S_R}{S_{IR} - S_R} = \frac{S_L - S_{L,Min}}{S_{L,Max} - S_{L,Min}} \quad (9)$$

where $S_{L,Min}$ and $S_{L,Max}$ are the minimum and maximum liquid saturations that correspond to the S_R and S_{IR}, respectively.

Fig. 4A shows triplicate experimental $P_C(S_{E,L})$ data points acquired using the new microfluidic system and the best fit $P_C(S_{E,L})$ curves for Toray TGP-H-090 for both liquid and gas intrusion. Table 2 presents the tabulated values of θ_{Mean} and σ from the best fits with the corresponding coefficient of determination (R^2). The calculation of R^2 is given in Appendix A. As the R^2 values show, both the liquid and gas intrusion curves fit the experimental data quite well, with 81% of the liquid intrusions experimental variance captured by the capillary model and 93% of the gas intrusion data variance captured by the model. Fig. 4B shows the resulting Ψ distributions that result from the best fit $P_C(S_{E,L})$ curves. Because the liquid intrusion $P_C(S_{E,L})$ data shows a significant volume of pores being both hydrophilic and hydrophobic, the resulting Ψ distributions are expected to sample a range of both hydrophilic and hydrophobic contact angles. Furthermore, since the majority of the pore volume is associated with pores on the order of $R_{Eff,i} \sim 10$ μm (see Fig. 2) the resulting $P_C(S_{E,L})$ curve is largely attributed to these pores with contact angle values

Table 2
Best-fit parameters for Toray TGP-H-090.

	θ_{Mean} (°)	σ (°)	R^2
Liquid intrusion	92	10	0.81
Gas intrusion	52	8	0.93

described by the Ψ function in Fig. 4B. Alternatively, the gas intrusion $P_C(S_{E,L})$ data show a majority of the pores being hydrophilic. As a result, Ψ is centered at a hydrophilic contact angle with low probability of finding a pore with $\theta > 90^\circ$. Examining the gas intrusion $P_C(S_{E,L})$ curve further shows an inflection at $S_{E,L} \sim 95\%$. This occurs because of the discrete combinations of $R_{Eff,i}$ and θ that can have $P_C \sim 0$ kPa. Based on Eq. (2), P_C on the order of a few kPa can only be achieved by having either large $R_{Eff,i}$ or $\theta \sim 90^\circ$. Because the Ψ distribution for gas intrusion does not extend to $\theta \sim 90^\circ$, the pores corresponding to $P_C \sim 0$ kPa can only come from the larger pores ($R_{Eff,i} > 10\ \mu m$) (see Fig. 2). Thus, the majority of the $P_C(S_{E,L})$ curve is attributed from $R_{Eff,i} \sim 10\ \mu m$ but pores with $R_{Eff,i} \sim 100\ \mu m$ dominate the curve at high saturations ($S_{E,L} > 90\%$).

From the data in Fig. 4A, we clearly observe hysteretic wetting between liquid and gas intrusion into the GDL. Hysteresis in the $P_C(S_L)$ curves was also observed in prior, less refined, experiments from our lab [20], and by Gostick et al. [21]. Because the pore structure of the GDL material is unlikely to change during liquid or gas intrusion, we assume all of the experimentally observed hysteresis in the $P_C(S_L)$ curves comes from hysteresis in the Ψ distribution, as shown in Fig. 4B and Table 2. Contact angle hysteresis is observed in most solid wetting processes unless extraordinary lengths are taken in surface preparation (smoothness, chemically homogeneous), regardless whether involving internal or external surfaces [14,15,24,29]. In fact, our external measurements of the advancing and receding contact angles on this material, Table 1, also shows strong hysteresis, as do prior external contact angle studies on other GDL materials [11]. Interestingly, hysteresis arises from the same chemical heterogeneity and surface roughness that we use to justify our Gaussian distribution of wetting angles [14,15,24,29]. Thus, the hysteresis in capillary properties that we observe here, previously [20], and in other labs [21] is further evidence of the complexity of GDL wetting.

Bundle of capillary models are known to have certain limitations. For example, interpretation of MIP data is affected by details of the porous geometry, such as pore bodies, throats, and connections [21], and these features are not fully captured in simple bundle of capillary models [14]. Nonetheless, bundle of capillary models are the dominant approach for interpreting MIP data and converting it into pore size distributions because the model captures many first-order effects. We anticipate similar issues from our use of bundle of capillary models to interpret capillary pressure data. The first-order effects this analysis reveals should significantly advance our ability to diagnose the processing–structure–property relationships that are essential for GDL design and manufacturing.

4. Conclusions and implications

We have shown an approach to deconvolute the influence of pore structure and internal wetting properties from $P_C(S_{E,L})$ measurements using a bundle of capillaries model. This work is the first to report representative contact angle (Ψ) distributions that describe the internal wetting properties of Toray TGP-H-090 for both liquid and gas intrusion that best fit experimental $P_C(S_{E,L})$ data. In our model we have taken into account the chemical heterogeneity and surface roughness of the GDL materials by assuming a single Gaussian distribution to describe Ψ. For a given pore size distribution, we have shown how different Ψ distributions can give rise to different $P_C(S_L)$ curves. In general, the mean contact angle θ_{Mean} shifts the magnitude of the P_C values and the contact angle standard deviation σ controls the slope and position of the ends of the $P_C(S_L)$ curves. By allowing θ_{Mean} and σ as free parameters, we found the representative Ψ distributions that allowed the bundle of capillaries model to best fit experimental $P_C(S_{E,L})$ data for both liquid and gas intrusion curve. Additionally, the Ψ distributions fall reasonably within the observed external contact angles measured. The combined experimental and modeling analysis we outline here provides a new way to link GDL wetting properties to the manufacturing of GDLs, and ultimately, should help design membrane electrode assemblies that are less prone to flooding. For example, this method may help understand the fundamental effects of Teflon® treatment on the resulting pore structure and surface properties in order to better determine the optimal Teflon® loading based on the desired properties. To galvanize the linkage between GDL processing–properties–performance, we have begun investigating the role of PTFE treatment and the effects of material aging on GDL capillary properties.

Acknowledgements

We would like to thank Tuesday Kuykendall for acquiring the MIP data and Jean St-Pierre (University of South Carolina) for his helpful discussions. This work was supported by the Boeing-Sutter Endowment for Excellence in Engineering.

Appendix A. Scaled sum of squares error and overall goodness of fit

A weighting is attached to a range of data points for the RSSE calculation. This is performed because the P_C data measured at $S_{E,L}$ around 0% and 100% have lower certainty due to complications with gas compression and expansion, respectively, present in the microfluidic cell. As a result, the P_C values corresponding to these saturation values have the least confidence. Thus, the data points within a range ΔP of $P_C(S_{E,L} = 50\%)$ are weighted by a factor of 10 while the remaining data points are unweighted shown by Eq. (A.1)

$$\mathrm{RSSE} = \begin{cases} \sqrt{\displaystyle\sum_{k=1}^{L} 10 \times \left(P_{C,k}\big|_{\mathrm{Expt}} - P_{C,k}\big|_{\mathrm{Model}} \right)^2} & \text{for } P_C(50\%) - \Delta P \le P_C \le P_C(50\%) + \Delta P \\ \sqrt{\displaystyle\sum_{k=1}^{L} \left(P_{C,k}\big|_{\mathrm{Expt}} - P_{C,k}\big|_{\mathrm{Model}} \right)^2} & \text{for all else} \end{cases} \tag{A.1}$$

with L being the total number of experimental P_C data points. It was found that ΔP of 4 kPa consistently captured the data with the most confidence quite well. Because the scaling procedure above weights certain points more heavily than others, based on experimental observations, it is important to ensure there remains an overall high quality fit. The overall goodness of these fits is assessed via an unweighted coefficient of determination (R^2), which describes the fraction of the total data variance captured by the best-fit model. It is computed as

$$R^2 = 1 - \frac{\displaystyle\sum_{k=1}^{L} \left(P_{C,k}\big|_{\mathrm{Expt}} - P_{C,k}\big|_{\mathrm{Model}} \right)^2}{\displaystyle\sum_{k=1}^{L} \left(P_{C,k}\big|_{\mathrm{Expt}} - \overline{P_C} \right)^2} \tag{A.2}$$

where

$$\overline{P_C} = \frac{\sum_{k=1}^{L} \left(P_{C,k}\big|_{Expt} \right)}{L} \tag{A.3}$$

Appendix B. Initial conditions for best fitting

Due to the highly nonlinear relationship between θ_{Mean} and σ to the generated $P_C(S_L)$ curve, the line searching process using the optimization toolbox tends to be locally trapped near the initial value at a local minima. In order to have higher confidence the local minima found is the close to the global minimum, different initial values spanning the range of each parameter was used. A total of 275 combinations were used to cover the spectrum of possible initial parameter values.

References

[1] C.Y. Wang, Chemical Reviews 104 (2004) 4727–4765.
[2] K. Tüber, D. Pócza, C. Hebling, Journal of Power Sources 124 (2003) 403–414.
[3] A. Bazylak, D. Sinton, N. Djilali, Journal of Power Sources 176 (2008) 240–246.
[4] X.G. Yang, et al., Electrochemical and Solid State Letters 7 (2004) A408–A411.
[5] F.Y. Zhang, X.G. Yang, C.Y. Wang, Journal of the Electrochemical Society 153 (2006) A225–A232.
[6] P.K. Sinha, P.P. Mukherjee, C.Y. Wang, Journal of Materials Chemistry 17 (2007) 3089–3103.
[7] A.Z. Weber, R.M. Darling, J. Newman, Journal of the Electrochemical Society 151 (2004) A1715–A1727.
[8] C.Y. Wang, in: H.A.G. Wolf Vielstich, Arnold Lamm (Eds.), Handbook of Fuel Cells—Fundamentals, Technology and Applications, John Wiley & Sons, Ltd., 2003, pp. 337–347.
[9] A.L. Dicks, Journal of Power Sources 156 (2006) 128–141.
[10] S.S. Kocha, in: H.A.G. Wolf Vielstich, Arnold Lamm (Eds.), Handbook of Fuel Cells—Fundamentals, Technology and Applications, John Wiley & Sons, Ltd., 2003, pp. 538–565.
[11] M.F. Mathias, in: H.A.G. Wolf Vielstich, Arnold Lamm (Eds.), Handbook of Fuel Cells—Fundamentals, Technology and Applications, John Wiley & Sons, Ltd., New York, 2003.
[12] C. Lim, C.Y. Wang, Electrochimica Acta 49 (2004) 4149–4156.
[13] J. Bear, Dynamics of Fluids in Porous Media, American Elsevier Pub. Co., New York, 1972.
[14] A.W. Adamson, Physical Chemistry of Surfaces, 5th ed., Wiley, New York, 1990.
[15] N.R. Morrow, The Journal of Canadian Petroleum Technology (1975) 42–53.
[16] J.T. Gostick, et al., Journal of Power Sources 156 (2006) 375–387.
[17] E.C. Kumbur, K.V. Sharp, M.M. Mench, Journal of the Electrochemical Society 154 (2007) B1315–B1324.
[18] E.C. Kumbur, K.V. Sharp, M.M. Mench, Journal of the Electrochemical Society 154 (2007) B1305–B1314.
[19] E.C. Kumbur, K.V. Sharp, M.M. Mench, Journal of the Electrochemical Society 154 (2007) B1295–B1304.
[20] J.D. Fairweather, et al., Electrochemistry Communications 9 (2007) 2340–2345.
[21] J.T. Gostick, et al., Electrochemistry Communications 10 (2008) 1520–1523.
[22] T.V. Nguyen, et al., Electrochemical and Solid-State Letters 11 (2008) B127–B131.
[23] W.G. Anderson, Journal of Petroleum Technology (1987) 1283–1300.
[24] F.A.L. Dullien, Porous Media Fluid Transport and Pore Structure, Academic Press, New York, 1979.
[25] N.R. Morrow, The Journal of Canadian Petroleum Technology (1976) 49–69.
[26] Y.M. Volfkovich, et al., Colloids and Surfaces A: Physicochemical and Engineering Aspects 187 (2001) 349–365.
[27] P.A. Webb, An Introduction to the Physical Characterization of Materials by Mercury Intrusion Porosimetry with Emphasis on Reduction and Presentation of Experimental Data, Micromeritics Instrument Corp., Norcross, GA, 2001.
[28] H.L. Ritter, L.C. Drake, Industrial Engineering Chemistry and Analytical Edition 17 (1945) 782–786.
[29] J.C. Berg, An Introduction to Surfaces, Colloids and Nanoscience, Department of Chemical Engineering, University of Washington, 2004.
[30] S. Baxter, A.B.D. Cassie, The Journal of the Textile Institute Transactions 36 (1945) T67–T90.
[31] M.C. Leverett, Transactions of the American Institute of Mining and Metallurgical Engineers (Incorporated) 142 (1941) 152–169.